SCIENCE CHINA
Information Sciences

August 2020, Vol. 63 180301:1–180301:16
https://doi.org/10.1007/s11432-019-2832-1

• RESEARCH PAPER •
Special Focus on mmWave and Terahertz Wireless Communications for B5G/6G

In-building coverage of millimeter-wave wireless networks from channel measurement and modeling perspectives

Peize ZHANG[1,3], Cheng YI[1,3], Bensheng YANG[1,3], Cheng-Xiang WANG[2,3], Haiming WANG[1,3*] & Xiaohu YOU[2,3]

[1]*State Key Laboratory of Millimeter Waves, Southeast University, Nanjing* 211111, *China;*
[2]*National Mobile Communications Research Laboratory, Southeast University, Nanjing* 211111, *China;*
[3]*Department of New Communications, Purple Mountain Laboratories, Nanjing* 211111, *China*

Received 29 December 2019/Accepted 16 March 2020/Published online 15 July 2020

Abstract To progress cost-effective deployment of millimeter-wave (mmWave) wireless networks for indoor users, the prediction of indoor-to-indoor (I2I) and outdoor-to-indoor (O2I) coverage based on field measurement studies is of great interest to the future generation mobile communication system. First, measurements in I2I and O2I scenarios, which have advantages in terms of achieving a fair comparison of channel characteristics across different mmWave bands and bandwidths, are performed. Next, the developed dual-slope path loss model with a break-point distance is found to well fit omnidirectional and directional measured I2I data, especially at 39.5 GHz, revealing that the transition from lit or shadow regions to totally blocked regions is abrupt. Combined with space-time propagation characteristics, the indoor blockage effect on path loss and angular spread is investigated, therein being essential for the design of beam-steering and tracking algorithms. Double-directional measurement results show that most dominant paths arrive along the line-of-sight path, and only a few in-building reflections can be detected in higher frequency bands. Based on the joint analysis of channel measurement and modeling results, several mmWave network design and in-building coverage enhancement insights are presented.

Keywords building entry loss, channel modeling, in-building coverage, millimeter-wave communication, propagation measurements

Citation Zhang P Z, Yi C, Yang B S, et al. In-building coverage of millimeter-wave wireless networks from channel measurement and modeling perspectives. Sci China Inf Sci, 2020, 63(8): 180301, https://doi.org/10.1007/s11432-019-2832-1

1 Introduction

Rapid changes in mobile communication technologies over the last ten years are in response to the remarkable growth of mobile data traffic given the advent of intelligent devices. The fifth-generation (5G) and beyond mobile communication systems are positioned to address the emerging demands, whereby millimeter-wave (mmWave) communication is considered as a promising technology for enabling multi-gigabit-per-second throughput and single-digit-millisecond latency [1–4].

mmWave communication, generally operating between 30 and 300 GHz, provides abundant spectrum resources and facilitates the miniaturization of radio frequency (RF) devices due to these shorter wavelengths. The severe propagation loss and high environmental sensitivities at mmWave bands, however,

* Corresponding author (email: hmwang@seu.edu.cn)

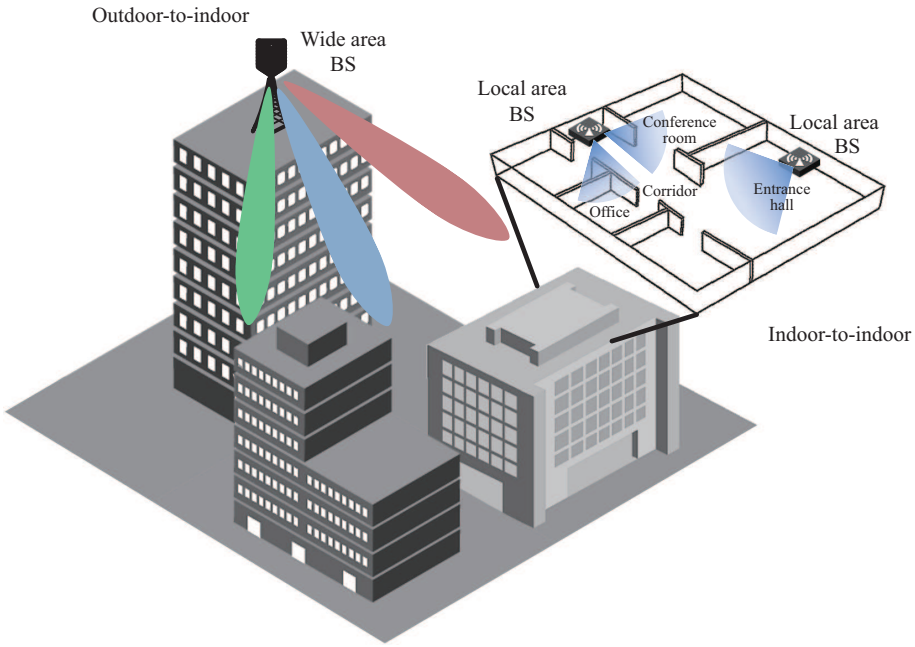

Figure 1 (Color online) Illustration of a potential mmWave indoor and outdoor cooperative cellular network for in-building coverage, including a highly directional beam in outdoor-to-indoor channels and a wide beam in indoor-to-indoor channels.

reduce the degree of flexibility in network deployments [5,6]. To overcome these challenges, beamforming techniques using large-scale antenna arrays have been promoted to track effective communication links based on the observation of directional channel characteristics, especially in non-line-of-sight (NLoS) scenarios [7,8]. Moreover, conventional macro base stations (BSs) operating below 6 GHz may be overlaid by massive mmWave micro or pico BSs with smaller cell radii. The cooperative transmission scheme for mmWave ultra-dense small cell networks is considered to simultaneously provide an extremely high data rate and reduce signal outages in indoor hotspot (InH) scenarios [9]. As shown in Figure 1, indoor mobile users can connect to either outdoor wide area BSs installed above the rooftops of surrounding buildings or indoor local area BSs in corridors or entrance halls, depending on the channel state information and access strategies. Therefore, to optimize the framework of in-building mmWave cellular systems toward achieving better network coverage and more efficient deployment of infrastructure, it is of great importance to obtain information about the mmWave channel characteristics in indoor-to-indoor (I2I) and outdoor-to-indoor (O2I) scenarios [10–13].

Recently, there have been multiple studies on indoor broadband channel measurements in two 5G mmWave bands, i.e., 28 GHz [14–16] and 39 GHz [17,18], mainly focusing on the characterization of propagation channels in several unique environments such as conference rooms, cubicle offices, corridors, and entrance halls. In-building measurement results show that the path loss exponents (PLEs) are generally smaller than the theoretical free space PLE of 2 under the line-of-sight (LoS) condition with vertical-to-vertical (V-V) polarimetric combination [15,17] due to the existence of rich multipath components (MPCs) reflected or diffracted from physical objects in the concerned environments [18,19]. However, conventional indoor path loss models for NLoS links, fitted via field measurement data using synthesized omnidirectional antennas, usually consider blocking effects as a part of shadow fading with larger PLEs [5,20]. There is a dearth of investigations considering the effect of building materials and structures on mmWave I2I transitions and small-scale channel characteristics in the literature except for [21,22], which is the basis of in-building coverage enhancement either for collocated antenna systems (CASs) or distributed antenna systems (DASs). For instance, mmWave CASs provide a feasible downlink transmission scheme under both LoS and NLoS conditions, where highly severe path loss in the NLoS I2I scenario requires compensation with a larger transmitted power; indoor DASs install multiple distributed

antennas within different semi-closed regions, therein not only reducing the average propagation distance between BSs and users but also generally producing LoS links inside each pico cell. Hence, the deployment of cost-effective indoor mmWave cellular networks considering propagation characteristics will be discussed further given the impact of transceiver siting, frequency, and bandwidth.

O2I coverage is the bridge between mmWave outdoor and indoor cellular networks and whose performance can be evaluated via isolated material penetration loss measurements or on-site cellular-type building entry loss (BEL) measurements [23]. Far-field penetration loss measurements are generally conducted using two identical narrow beamwidth horn antennas with the material under test (MUT) located perpendicular to the transmitter-receiver (T-R) boresight, wherein the distance between the MUT and each antenna must be larger than the far field distance [24]. The measurement results in different practical scenarios have shown material-dependent behavior and frequency dependencies with fluctuations [24,25]. On the other hand, the BEL is an excess loss relative to the log-distance path loss model due to users being inside buildings. For cellular-type O2I channel measurements following the standard instructions in [26], multiple reflected and diffracted MPCs from surrounding physical objects can be extracted [27–29], thereby providing a more practical network deployment in comparison with far-field measurements. The BEL models proposed by the ITU-R study group 3 [30] and 3GPP [31] provide experimental parameters to characterize the impact of frequency, non-perpendicular incidence, and building type on the overall propagation loss. However, only a handful of researchers are devoted to the space-time propagation characterization of mmWave O2I channels [32,33], which has a further effect on outdoor cellular network deployment for in-building coverage.

In this paper, to evaluate the performance of outdoor and indoor mmWave cellular systems with continuous coverage, empirical analysis of I2I and O2I channel characterization with a focus on large-scale and small-scale channel characteristics is presented. The measurement-based path loss and space-time channel models across different frequencies and bandwidths in indoor environment are derived. In contrast to the analysis in [14–18], the transition from shadow regions to totally blocked regions is studied in terms of directional and omnidirectional path loss, delay spread (DS), and azimuth angular spread of arrival and departure (ASA/ASD). The bandwidth dependency of channel parameters are discussed with a focus on the impulse dispersion of multipath channels. Empirical comparison of propagation characteristics in different regions reveals the blockage effects on coverage analysis for indoor mmWave cellular networks. Thanks to the employment of a flexible mmWave channel sounder using double-directional scanning pattern [34], the beamspace directional channel characteristics for the O2I scenario across 27.5 and 39.5 GHz are investigated. Apart from the analysis of BEL versus receiver (RX) location, the directional sounding data are leveraged to extend the spatial characterization of O2I channels. The joint analysis of channel characteristics and models in I2I and O2I scenarios, incorporating the impact of the transceiver siting and physical blockages, enables optimal in-building coverage under outdoor and indoor cooperative transmission schemes.

The remainder of this paper is organized as follows. Section 2 details the measurement environments, setup, and procedures. Sections 3 and 4 report the statistics of the large-scale and small-scale propagation characteristics for indoor and O2I channels, respectively. Based on field measurement results, some implications concerning the deployment planning of in-building cellular networks are also presented. The conclusion is drawn in Section 5.

2 Measurement setup and methodology

2.1 Outdoor-to-indoor channel measurements

The double-directional O2I channel measurement campaign was conducted in China network valley (CNV), Nanjing, China in the spring of 2018 using a custom-designed channel sounder based on commercial off-the-shelf (COTS) instruments. A detailed description of our flexible wideband mmWave channel sounders can be found in [34]. The sounding signal is a 4096-length Golay complementary sequence with

Table 1 Antenna specifications for mmWave O2I and indoor channel measurements

Parameter	Value	
Carrier frequency	27.5 GHz	39.5 GHz
TX/RX ant. HPBW[a)]	9.5°(Az.)/9.5°(El.)	9.5°(Az.)/9.5°(El.)
TX/RX ant. gain	25.6 dB	27.7 dB
Pol. combination	V-V	
TX ant. azimuth angle	O2I: 60° with increment of 10°; Indoor: 90° with increment of 10°	
TX ant. elevation angle	O2I: −10°; Indoor/penetration: 0°	
RX ant. azimuth angle	O2I/Indoor: 360° with increment of 10°	
RX ant. elevation angle[b)]	O2I: −10°, 0°, 10°; Indoor: 0°, 10°	

a) HPBW means the half power beamwidth for the high-gain horn antennas.

b) The RX elevation angles were selected based on the topologies of the concerned environments and measurement configurations (e.g., TX and RX antenna heights and TX antenna downtilt).

the RF null-to-null bandwidths of 200 and 600 MHz[1)], while the measurable path loss can be respectively up to 158 and 155 dB at 27.5 GHz, deembedding the antenna radiation pattern and amplifier gains. Two external GPS rubidium (Rb) standard references are utilized for frequency synchronization and triggering data acquisition. The system is equipped with two pairs of horn antennas operating at 27.5 and 39.5 GHz, respectively, which can be mechanically steered in the azimuth and elevation dimensions to emulate a beam scanning and tracking scheme. Table 1 shows the antenna specifications as well as their rotational range. Calibrations are performed by back-to-back measurements while transmitter (TX) and RX are connected via a variable attenuator of 75 dB to capture sounder's impulse responses, which can be deembeded in post-processing [34]. During measurements, all instruments are connected through a wireless local area network (WLAN) and controlled automatically by the custom-designed software.

Figure 2 depicts one TX location on the rooftop of Building A3 (R-TX) with the TX antenna height set to 15 m above the ground, and 23 indoor RX locations (O-RXs) on the third floor of Building A5, which consists of a reinforced concrete frame structure and was remodeled into a closed office environment with cubicle offices, conference rooms, corridors, and halls. As shown in Figure 2, the external building wall is composed of brick and concrete with standard double-pane windows, and the window-to-wall ratio is approximately 2:1. Additionally, O-RX 1–15 are located in a modern office (11.7 m × 8.3 m × 2.9 m) with typical office furniture (such as desks, chairs, cubicles, and cabinets), and O-RX 16–23 are located in corridors that are separated from the inside RXs via glass partition walls and composite doors. The spatial density of points has been carefully considered to ensure that these RXs are uniformly distributed and able to collect sufficient channel data from all the unique aspects of the building.

2.2 Indoor channel measurements

For the cellular-type indoor channel measurement campaign, the same COTS-based sounder was utilized. The specifications of the antennas are also reported in Table 1. To investigate the relationship between fading and bandwidth for the mmWave multipath channel, two different bandwidths (i.e., 200 and 600 MHz, corresponding to 10 and 3.3 ns delay resolutions, respectively) are also configured consistent with the O2I channel measurement campaign. The measurements were performed on the third floor of Building A3, which shares the same structure as Building A5 for the O2I measurements. The heights of TX and RX antennas are 1.9 and 1.8 m, respectively. Figure 3 depicts the layout of indoor transceiver locations, where I-TX is in the hall, 15 I-RXs are in the corridor (NLoS case 1), and 16 I-RXs are in the conference room or cubicle offices (NLoS case 2). Typically, a metal door exists south of the corridor 70.5 m away from I-TX. Note that all RX locations are in NLoS scenario and composite doors are closed during the measurements.

1) Note that transmitted sequence is stated at the clock rate of 100 and 300 MHz, and the aftermentioned bandwidth denotes the RF null-to-null bandwidth.

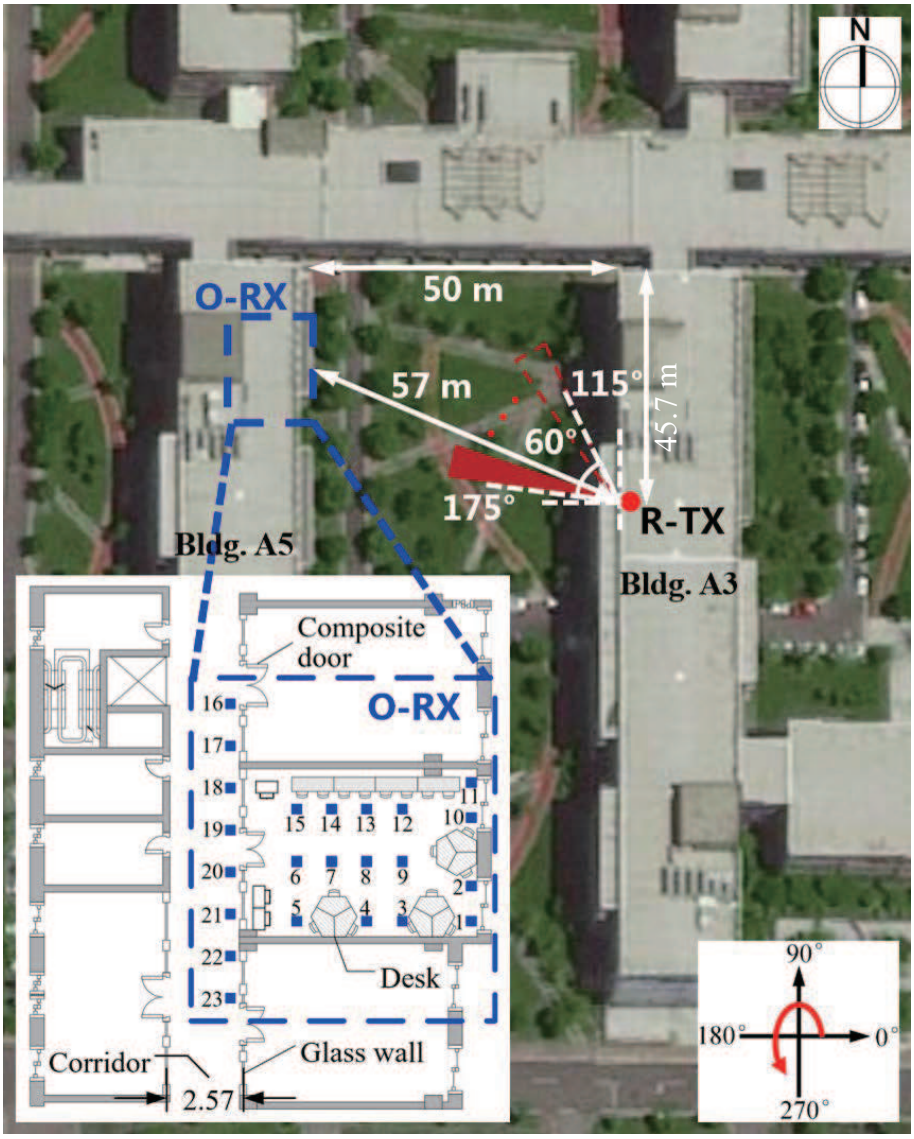

Figure 2 (Color online) General plan view of O2I scenario. The TX is mounted on the rooftop of Building A3, and indoor RXs are located on the third floor of Building A5, which are all in the illuminated area.

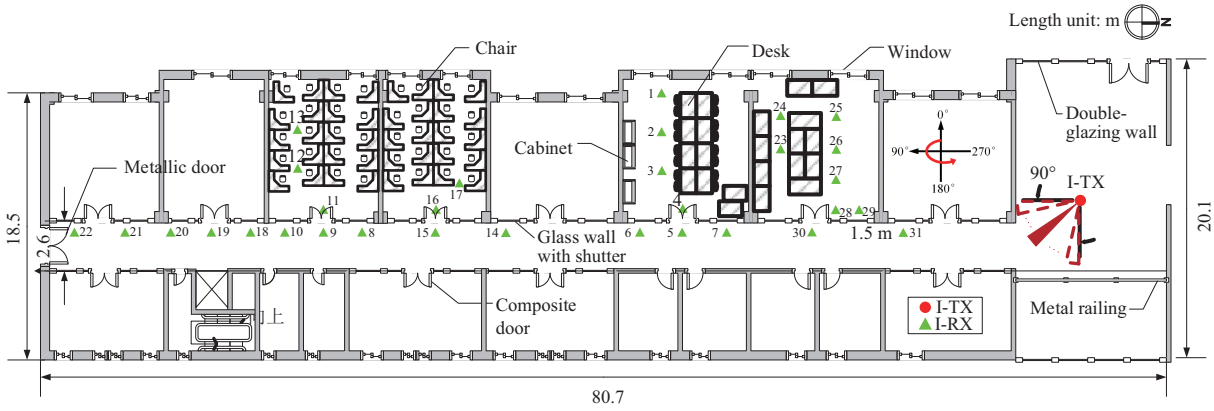

Figure 3 (Color online) Layout of indoor TX and RX locations, where the red dots and green triangles represent the TX and RX locations for the indoor measurements, respectively.

3 Indoor channel characterization

3.1 Path loss and shadow fading

The calculation of path gain is first considered based on directional sounding data and the power delay profiles (PDPs) are compared for different channel bandwidths. After that, a dual-slope path loss model is proposed for mmWave indoor transitional propagation.

3.1.1 *Channel data processing*

Let $h(\tau, \boldsymbol{\Theta}, \boldsymbol{\Phi})$ be the directional channel impulse response (CIR) at the vector of the azimuth and elevation angle of departure (AoD/EoD) $\boldsymbol{\Theta} = (\theta, \phi)_{\mathrm{TX}}$ and the vector of the azimuth and elevation angle of arrival (AoA/EoA) $\boldsymbol{\Theta} = (\theta, \phi)_{\mathrm{RX}}$, which has deembedded sounder impulse responses obtained through back-to-back calibration measurement. In particular direction, each CIR is averaged over seven snapshots to smooth noise floor and then directional PDP $P(\tau, \boldsymbol{\Theta}, \boldsymbol{\Phi}) = |h(\tau, \boldsymbol{\Theta}, \boldsymbol{\Phi})|^2$ is obtained. The received power of narrow beam is defined as [35]

$$p_{\boldsymbol{\Theta},\boldsymbol{\Phi}} = \int_{\tau_0}^{\tau_1} P(\tau, \boldsymbol{\Theta}, \boldsymbol{\Phi})\, \mathrm{d}\tau, \tag{1}$$

where τ_0 and τ_1 denote the first and last time for the PDP exceeding the noise floor, respectively, which can be extracted following the method proposed in [36, 37]. To remove the influence of noise, a margin of 10 dB above the noise floor, calculated as the variance of last hundred ns of CIR, is chosen to filter the PDP samples whose magnitude is below this level and these invalid samples are all set to zero. Consequently, the omnidirectional received power is non-coherently combined as [10]

$$P_{\mathrm{omni}} = \sum_{\boldsymbol{\Theta}} \sum_{\boldsymbol{\Phi}} p_{\boldsymbol{\Theta},\boldsymbol{\Phi}}. \tag{2}$$

Figure 4 presents examples of directional PDPs measured at I-RX 5 with RF bandwidths of 200 and 600 MHz at 27.5 GHz. The noise floor for the case of 200 MHz bandwidth is 5.56 dB lower than the case of 600 MHz bandwidth, which is close to the theoretical difference of $10\log_{10}(600/200) = 4.77$ dB. Therefore, the dynamic range of the COTS-based sounder decreases with increasing signal bandwidth, leading to less detectable MPCs with relatively low received power and large propagation delay. On the other hand, the time delay resolution is equal to $2/B$ where B denotes RF null-to-null bandwidth; and in turn, a reduction in sounding signal bandwidth corresponds to a reduction in delay resolution, which results in multipath smearing for mmWave sparse channel. For example, if the threshold value of 30 dB below the peak level of the PDP is used as shown by the inset in Figure 4, two time clusters (following the definition in [38]) can be found with delay resolution of 3.3 ns but only one in the case of 10 ns delay resolution. Thus, physical multipath clusters that share similar cluster delay cannot be distinguished using narrow sounding bandwidth for mmWave channels.

3.1.2 *Dual-slope path loss model*

The field-measured path loss in the mmWave band is generally fit with two fundamental single-slope models: the close-in (CI) free-space reference distance model and the floating intercept (FI) model [10]. The CI model provides a fair comparison of the path loss measurement results in terms of the PLE across different configurations such as frequency, bandwidth, and transceiver siting. In the FI model, more model parameters are estimated via a least-squares regression to provide the line of best fit to the data points, although it has no physical basis compared with the CI model [10]. However, despite these two models characterize path loss varying with the T-R separation distance in simple environments, they ignore the blockage effect when the RX locations are isolated via environmental obstacles. Thus, a dual-slope path loss model with a break-point (BP) distance of d_{BP} is adopted, and it is expressed as

$$L(d) = \begin{cases} L_0(d_0) + 10\alpha_0 \log_{10}(d/d_0) + X_{\sigma_0}, & d \leqslant d_{\mathrm{BP}}, \\ L(d_{\mathrm{BP}}) + \beta_1 + 10\alpha_1 \log_{10}(d/d_{\mathrm{BP}}) + X_{\sigma_1}, & d > d_{\mathrm{BP}}, \end{cases} \tag{3}$$

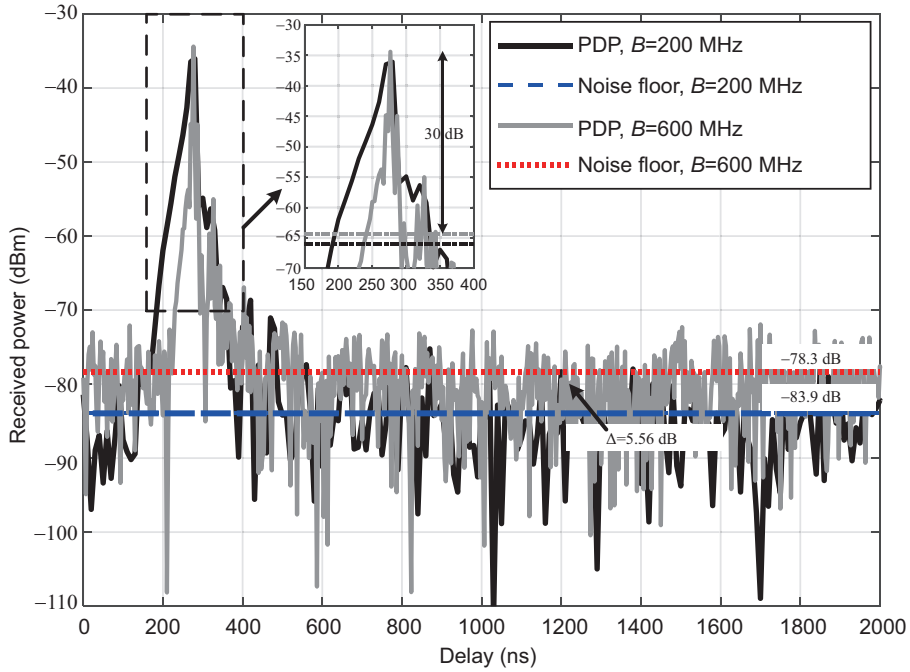

Figure 4 (Color online) Comparison of the measured directional PDPs for I-RX 5 at 27.5 GHz with bandwidths of 200 (black line) and 600 MHz (gray line).

where $L_0(d_0) = 20\log_{10}(4\pi d_0/\lambda)$ is the free-space path loss (FSPL) at a reference distance of $d_0 = 1$ m, α_0 is the PLE, α_1 and β_1 are the optimized slope and intercept, respectively, while σ_0 and σ_1 in dB are the standard deviations of the zero-mean-Gaussian-distributed shadow fading components. Note that d denotes the propagation distance rather than the Euclidean distance between TX and RX, which ensures a precise path loss estimation or link budget in an NLoS setting.

The path loss model in (3) becomes a CI model at $d \leqslant d_{\rm BP}$, where the set (α_0, σ_0) is obtained through a minimum mean square error fit to the measurement data in the lit region (i.e., LoS scenario) or shadow region (i.e., deep fading due to reflection and diffraction) [17]. Specifically, they are fitted based on the data measured in NLoS case 1. For the post-BP segment, the FI model is fit to the difference of $L(d) - L(d_{\rm BP})$, where the path loss at the BP distance can be computed as

$$L(d_{\rm BP}) = L_0(d_0) + 10\alpha_0 \log_{10}(d_{\rm BP}/d_0) \tag{4}$$

or substituted by the reference measurement or ray-tracing simulation results. In this work, $L(d_{\rm BP})$ is computed following (4). The parameter β_1 denotes the I2I excess loss relative to $L(d_{\rm BP})$ due to physical obstruction by building materials. The FI model can give the best fit to the data points for blocked NLoS links at $d > d_{\rm BP}$. Such a dual-slope path loss model can apply to complicated propagation environments with blockages.

3.1.3 *Results and analysis*

To provide an intuitive comparison of the CI model and improved dual-slope model, the conventional CI model is first used to fit the measured data in NLOS case 1 and 2, respectively. As shown in Figure 5, the directional path loss in the NLoS case 2 is much greater than the results in the case 1, due to existing physical blockages. Note that in the case 1 the PLE for the best single beam combinations between TX and RX antennas at 27.5 GHz is much larger (PLE = 3.5), and is reduced to PLE = 2.9 when directional received power is non-coherently combined for omnidirectional channel modeling. In comparison with the results at 28 GHz [15], PLEs are 3.0 for NLoS-best setting and 2.7 for omnidirectional setting; however, they provide rather large standard deviations in both settings. It is speculated that relatively smaller PLEs in [15] may be due to the absence of measured data over a wide range (e.g., within 45.9 m T-R

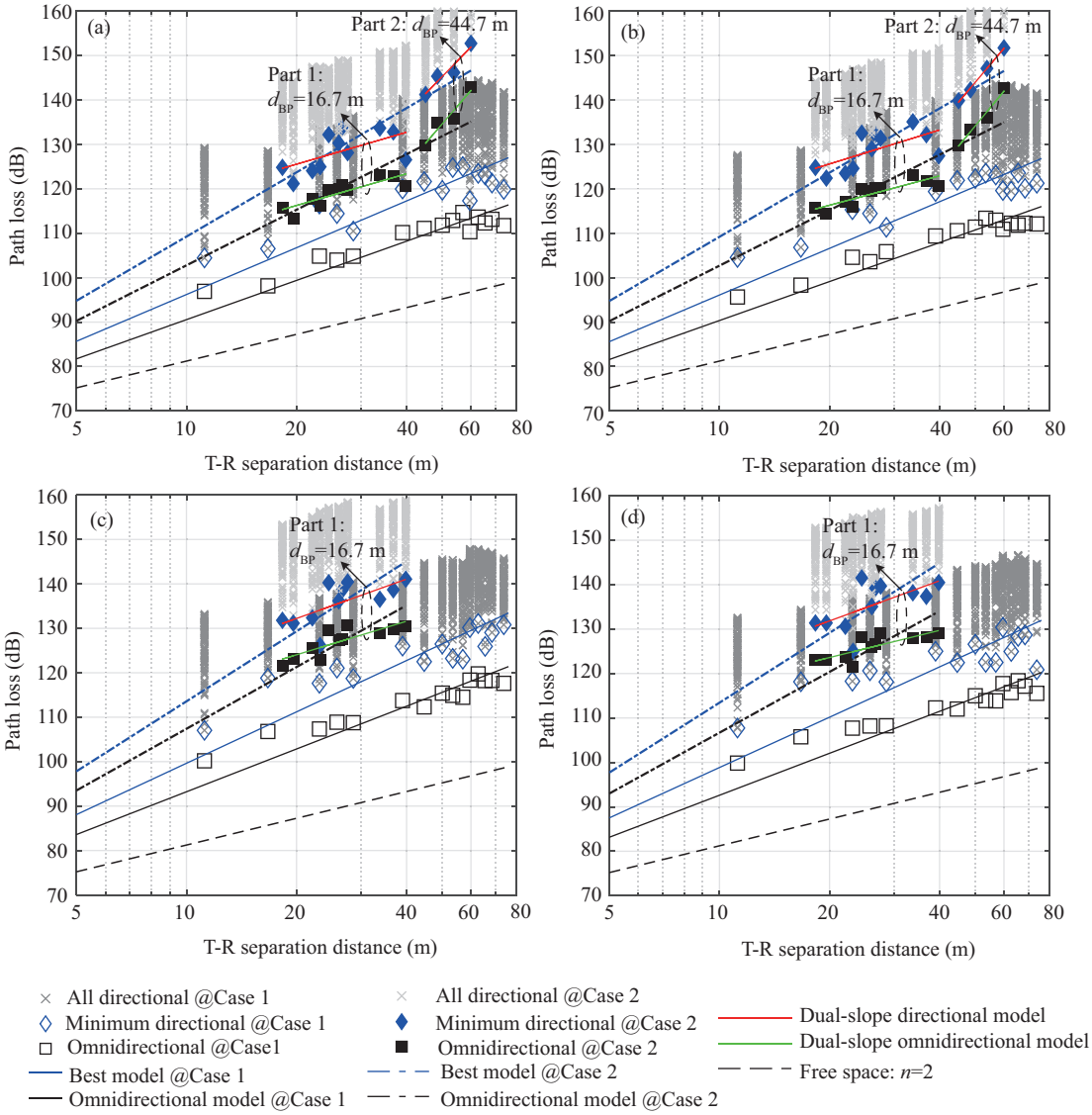

Figure 5 (Color online) Measured directional and omnidirectional path loss for all I-RX locations, as well as their fitting results. The gray crosses represent the top 80 directional path loss values over all 720 antenna pointing angle combinations (10 AoD × 36 AoA × 2 EoA), the blue diamonds represent the path with the strongest received power, i.e., the lowest directional path loss, and the black squares represent omnidirectional path loss. (a) and (b) represent 27.5 GHz with RF bandwidths of 200 and 600 MHz, respectively, as well as (c) and (d) in 39.5 GHz band.

separation distances) whereas path loss data generally increases rapidly with propagation distance [19]. Additionally, all NLoS measurement data was utilized (similar to the combination of cases 1 and 2 in this work), corresponding to much larger standard deviations. The multi-frequency measurement results for the NLoS link also indicate that the PLE and shadow fading variance increase with frequency. Considering the impact of transceiver siting, received signals are mainly reflected from smooth glass walls and diffracted over the 90° wall corner, leading to pronounced reduction of received signal strength with increasing frequency and incident angle [39]. On the other hands, slight differences of path loss across two sounding bandwidths at identical frequency partly confirm that large-scale parameters are independent of bandwidth [40]. By comparing the omni- and best-directional path loss models, it is seen that significant space diversity gain can be obtained after beam combining, meaning that beam scanning scheme must be implemented within a wider angle range to enhance the coverage of indoor mmWave systems.

The BP path loss models can be visualized in Figure 5, and their corresponding model parameters are detailed in Table 2. The BP is set to the reference location at I-RX 30 with d_{BP} of 16.7 m (part 1)

Table 2 Path loss model parameters in indoor NLOS setting at 27.5 and 39.5 GHz with $d_{\mathrm{BP}} = 16.7$ m for part 1 and $d_{\mathrm{BP}} = 44.7$ m for part 2

Frequency (GHz)	B (MHz)	Scenario	The CI path loss model								Dual-slope path loss model					
			Case 1		Case 1		Case 2		Case 2		Case 2			Case 2		
			Best direction		Omnidirection		Best direction		Omnidirection		Best direction			Omnidirection		
			α_0	σ_0	α_0	σ_0	α_0	σ_0	α_0	σ_0	α_1	β_1	σ_1	α_1	β_1	σ_1
27.5	200	Part 1	3.5	4.2	2.9	2.5	4.8	4.3	4.2	3.4	2.4	19.7	3.6	2.4	17.3	1.6
		Part 2									8.5	22.1	1.3	9.6	20.3	1.6
	600	Part 1	3.5	3.9	2.9	2.3	4.8	3.9	4.2	3.3	2.5	19.7	3.3	2.2	17.7	1.4
		Part 2									9.8	20.4	0.3	10.0	19.9	1.0
39.5	200	Part 1	3.8	4.6	3.2	2.8	5.2	4.4	4.6	2.9	2.9	21.7	3.6	2.5	21.7	1.9
	600	Part 1	3.8	5.5	3.1	3.0	5.2	4.7	4.6	3.2	3.0	22.3	4.1	2.0	22.4	1.7

and I-RX 15 with d_{BP} of 44.7 m (part 1)[2)]. The set (α_0, σ_0) is substituted by the CI model parameters in the NLoS case 1. It is seen that the step loss values β_1 are all positive due to the channel transition from deep fading region to totally blocked region and strictly increase with increasing carrier frequency. In comparison with the traditional CI models, pronounced differences can be observed in the case 2 and the dual-slop path loss models fit well with the measured data (see green and red lines in Figure 5). Moreover, remarkably small shadow factors σ_1 for various settings as evident from Table 2, in comparison to the results obtained using the single-slope models [15,16], indicate that the proposed model regarding propagation distance is appropriate for path loss prediction in totally blocked indoor NLoS scenarios. Much smaller slopes α_1 relative to α_0 for the part 1 segment are observed, meaning that path loss does not increase as fast as the CI model predicting in transition regions and it will underestimate the cell range of mmWave systems. However, measurement results show that if indoor blockages are far from TX, path loss will rapidly increase (i.e., part 2) corresponding to the reduction of in-building coverage.

3.2 Delay and angular spreads

Besides the large-scale path loss model, the small-scale space-time propagation model is also of great importance for mmWave cellular network planning with cost-effective coverage. The omnidirectional small-scale fading characteristics are preferred in current mmWave channel models [31] since arbitrary antenna array patterns can be employed with omnidirectional models. The root-mean-square (RMS) DS is defined as the second central moment of the PDP [20]:

$$\tau_{\mathrm{RMS}} = \sqrt{\frac{\sum_i \tau_i^2 P(\tau_i)}{\sum_i P(\tau_i)} - \left(\frac{\sum_i \tau_i P(\tau_i)}{\sum_i P(\tau_i)}\right)^2}, \tag{5}$$

where τ_i and $P(\tau_i)$ $(i = 1, \ldots, M)$ are the delay and path power of the ith MPC and M is the number of effective MPCs. The omnidirectional PDPs $P(\tau)$ are synthesized via directional PDPs $P(\tau, \boldsymbol{\Theta}, \boldsymbol{\Phi})$

$$P(\tau) = \sum_{\boldsymbol{\Theta}} \sum_{\boldsymbol{\Phi}} P(\tau, \boldsymbol{\Theta}, \boldsymbol{\Phi}), \tag{6}$$

where precise time synchronization enables the independent combination of directional radio channels. The RMS ASA is defined as the second-order central moment of the azimuth angular power spectrum (APS) $P(\phi_{\mathrm{RX}})$ [41]:

$$\phi_{\mathrm{RX,RMS}} = \sqrt{\frac{\sum_j \left|\exp(j\phi_{\mathrm{RX},j}) - \overline{\theta}_{\mathrm{RX}}\right|^2 P(\phi_{\mathrm{RX},j})}{\sum_j P(\phi_{\mathrm{RX},j})}} \tag{7}$$

2) The RX locations in conference rooms belong to part 1, including I-RX 1–4 and 23–29; the RX locations in cubicle offices belong to part 2, including I-RX 11–13, 16, and 17.

Table 3 Statistics of composite delay and angular spreads in indoor NLoS setting at 27.5 and 39.5 GHz

Frequency (GHz)		27.5				39.5			
B (MHz)		200		600		200		600	
Scenario		Case 1	Case 2	Case 1	Case 2	Case 1	Case 2	Case 1	Case 2
Composite DS	μ	−7.2	−7.4	−7.1	−7.2	−7.3	−7.5	−7.2	−7.4
($\log_{10}$(s))	σ	0.11	0.12	0.06	0.04	0.06	0.09	0.05	0.08
Composite ASA	μ	1.6	1.7	1.6	1.7	1.5	1.6	1.6	1.7
($\log_{10}(^\circ)$)	σ	0.13	0.03	0.13	0.04	0.13	0.08	0.13	0.06
Composite ASD	μ	1.3	1.1	1.3	1.1	1.3	1.1	1.3	1.1
($\log_{10}(^\circ)$)	σ	0.09	0.16	0.09	0.16	0.09	0.09	0.09	0.08

with mean angle

$$\overline{\phi}_{\mathrm{RX}} = \frac{\sum_j \phi_{\mathrm{RX},j} P\left(\phi_{\mathrm{RX},j}\right)}{\sum_j P\left(\phi_{\mathrm{RX},j}\right)}, \tag{8}$$

where $P\left(\phi_{\mathrm{RX}}\right)$ is obtained based on directional received power over the entire 360° azimuth plane and $\phi_{\mathrm{RX},j}$ $(j = 1, \ldots, 36)$ is the rotating angle with the resolution of 10°.

Table 3 reports the statistics of the RMS delay spread following log-normal distribution based on beam combining results. For the frequency-dependent effect, the mean values of the RMS DS strictly reduces with frequency while the RMS ASA and ASD in general show the similar behavior in different measurement settings. This is a distinguishing feature of mmWave radio propagation, which becomes sensitive to surrounding objects with comparable roughness to the wavelength. Similar results have also been observed in [15, 16] in the ranges of 28–73 GHz and 2.9–61 GHz, respectively. Due to the impact of sounding bandwidth, the means of τ_{RMS} generally increase with increasing channel bandwidth (e.g., 66.08 and 84.95 ns in case 1 at 27.5 GHz with RF bandwidths of 200 and 600 MHz, respectively; and 40.45 and 64.05 ns in case 2 at 27.5 GHz). Additionally, the τ_{RMS} in case 1 are all larger than the results in case 2 under different measurement configurations (i.e., carrier frequency and bandwidth). This may be due to the fact that the RXs in case 2 are blocked by glass walls and composite doors such that less detectable MPCs are received within a limited time duration. Based on a detailed study of these results, following conclusion can be drawn: (1) the measured DS for the NLoS link increases with increasing channel bandwidth due to the better delay resolution, and (2) the transition from the NLoS over a corner to the totally blocked NLoS region (i.e., from case 1 to case 2) will result in a smaller DS.

As identified in (7) and (8), the angular spread is computed based on the APS which is synthesized via directional received power, while no clear trend can be observed between large-scale channel characteristics and bandwidth [40]. Combining with our field measured results reported in Table 3, the relationship between the average ASA or ASD value and bandwidth is also not obvious; in other words, azimuth angular spreads seems to be bandwidth-independent. In contrast to τ_{RMS}, the means of $\phi_{\mathrm{RX,RMS}}$ follow an opposite trend which increases with RX moving to the locations in case 2. This increase is because the signals transmitted from NLoS I-TX will experience strong reflection from both sides of the corridor and diffraction over the 90° wall corner; consequently, more signals from multiple directions will penetrate in-building obstacles into the interiors. Figure 6 presents the 27.5 GHz double-directional APSs with different modifications. Note that directional received power in each azimuthal direction of departure and arrival is combined across two elevations of −10° and 0°. Apparently, signals transmitted from NLoS I-TX concentrate in a relatively narrow AoD range of $[120^\circ, 150^\circ]$. At case 1 RX side, first- and second-order reflected paths are dominant which are forced into a limited angular range at the ϕ_{RX} of 260° and with RX moving away from I-TX, high-order reflections from the metal door on the north side of the corridor become more strong (compared Figure 6(b) and (d)). However, for the totally blocked RX region, received signals are mainly from the forward paths penetrating the glass partition walls, while inside reflections are almost undetectable. An example of such condition for RX 28 is shown in Figure 6(e) and (f), where the maximum directional received power from the ϕ_{RX} of 230° is about 20 dB lower than the results for RX 30 with approximate the same T-R separation distance. Hence, it is reasonable to

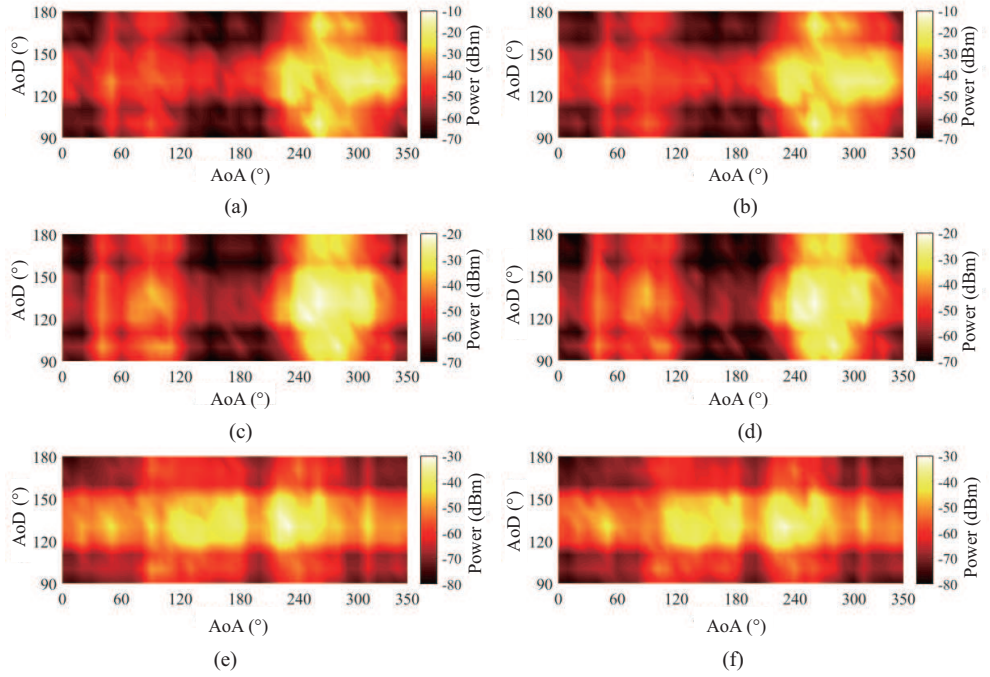

Figure 6 (Color online) Double-directional APS at 27.5 GHz. (a) and (b) for RX 30 with bandwidths of 200 and 600 MHz, respectively, as well as (c) and (d) for RX 5 and (e) and (f) for RX 28.

conclude that when using directional antennas for indoor coverage, adjustments of the beam orientation in the azimuthal direction will induce greater multipathing for I2I channels.

4 Outdoor-to-indoor coverage analysis

4.1 Omnidirectional building entry loss

In this subsection, cellular-type BEL measurement results are analyzed and the effects of RX position, carrier frequency, and signal bandwidth on O2I channel characteristics are discussed.

The BEL is defined as the additional propagation loss when outdoor BSs provide wireless coverage for users inside a building [26]. Despite sufficient site-specific penetration loss measurements have been conducted at multiple mmWave bands [24,25], there are only few cellular-type measurements considering double-directional spatial propagation. In this work, thousands of double-directional PDPs are collected based on the O2I channel measurements at 27.5 and 39.5 GHz with RF bandwidths of 200 and 600 MHz, therein yielding detailed studies of omnidirectional and directional channel characteristics in the O2I scenario. The BEL at each O-RX location is calculated by

$$L_{\mathrm{BE}}(d) = L(d) - L_0(d), \tag{9}$$

where $d = d_{\mathrm{out}} + d_{\mathrm{in}}$ is the Euclidean distance between TX and RX and consists of two parts (i.e., outdoor d_{out} and indoor d_{in}). Note that there are no obstacles between R-TX and the facade of Building A5, which simulates a practical installation of an O2I wireless communication network. $L(d)$ and $L_0(d)$ can be calculated following the method presented in Subsection 3.1.

Figure 7 shows the measurement-based omnidirectional BEL for different settings, where the color of the square indicates the BEL at each O-RX location. It is clear that the BEL for the C-RX nearest to the external wall and window is smaller than that for the C-RX on the side of the office further from the R-TX, albeit with some exceptions. For example, the BEL at O-RX 14 is obviously lower than the results at surrounding O-RXs because its location is in line with the incident direction and the penetration loss for double-pane glass windows is significantly smaller than that for brick walls [22]. To study the

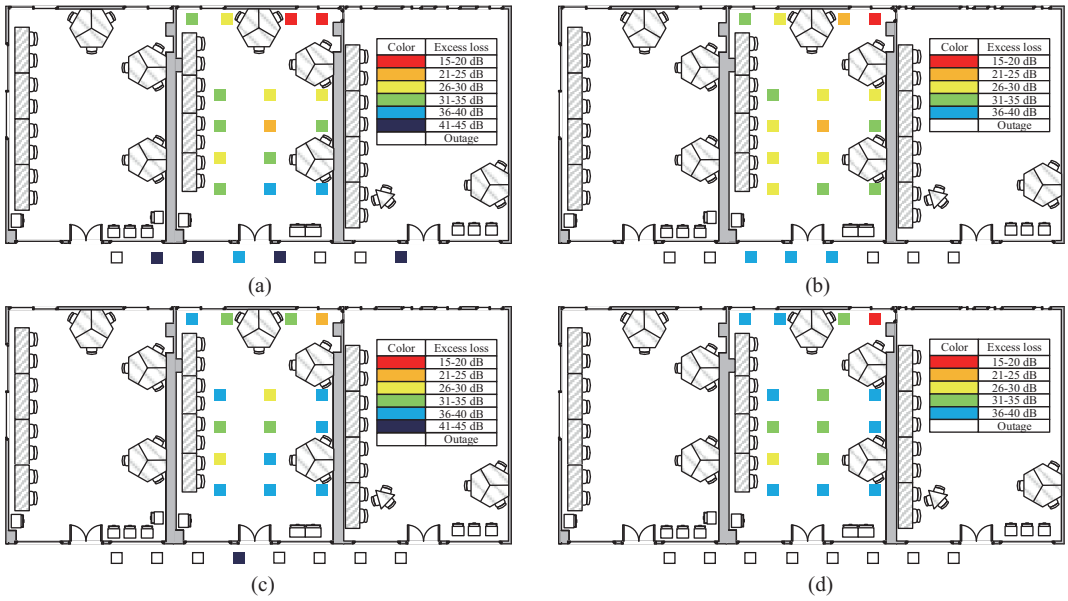

Figure 7 (Color online) Excess losses relative to free space path losses for all O-RX locations. (a) and (b) at 27.5 GHz with bandwidths of 200 and 600 MHz, respectively, as well as (c) and (d) at 39.5 GHz.

Table 4 Statistics of O2I omnidirectional channel parameters for O-RXs inside the office

Frequency (GHz)		27.5		39.5		28 [33]	28 [42]
Bandwidth (MHz)		200	600	200	600	400	0.02
BEL (dB)	Maximum	33.3	32.1	38.6	38.9	–	–
	Minimum	16.1	15.1	20.91	19.3	–	–
	Average	27.5	25.9	32.3	32.8	22.7	17.1
	Standard	5.3	4.6	4.9	4.9	1.2	2.8
	$\rho_{\mathrm{BEL},d_{\mathrm{in}}}$	0.54	0.49	0.33	0.28	–	–
ASA (°)	Average	83.9	79.1	78.8	63.5	37.5	–
	Standard	52.6	57.5	51.2	58.8	–	–
ASD (°)	Average	7.6	7.3	7.2	6.8	–	–
	Standard	2.0	2.1	2.2	3.0	–	–

cross-correlation properties between L_{BE} and d_{in}, the cross-correlation coefficients can be computed as

$$\rho = \frac{\mathrm{E}\{(L_{\mathrm{BE}} - \overline{L}_{\mathrm{B}})(d_{\mathrm{in}} - \overline{d}_{\mathrm{in}})\}}{\sqrt{\mathrm{E}\{(L_{\mathrm{BE}} - \overline{L}_{\mathrm{B}})^2\}\,\mathrm{E}\{(d_{\mathrm{in}} - \overline{d}_{\mathrm{in}})^2\}}}, \tag{10}$$

where $\overline{L}_{\mathrm{B}}$ and $\overline{d}_{\mathrm{in}}$ are the mean values of the BEL and d_{in} datasets, respectively, and $\mathrm{E}\{\cdot\}$ is the expectation operator. Table 4 reports the cross-correlation coefficients based on measured data, which suggest positive correlations between the BEL and the indoor propagation distance d_{in}. According to Table 4, the omnidirectional BELs at 27.5 GHz are significantly correlated to d_{in} and become slightly correlated at 39.5 GHz. Therefore, the BEL is mainly determined by the RX locations and building structures. The statistics of the BEL over all C-RXs in the office are also detailed in Table 4. The differences between the maximum and minimum BELs for the four configurations are approximately 18 dB, corresponding to larger standard deviations. On the other hand, slight differences between the BEL measured with different sounding bandwidths can be observed, which is in agreement with the findings for I2I channels. Compared with the BEL measurement results reported in [33, 42], the omnidirectional BELs and their standard deviations in this work are much larger due to having metal railings outside the windows.

The BEL measurement results illustrate that mmWave signals penetrating through the building blockages undergo substantial attenuation. Hence, the cooperative transmission between outdoor and indoor

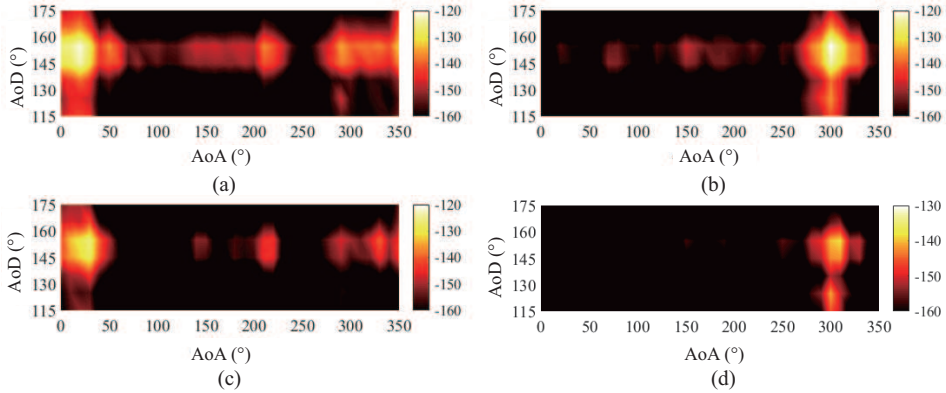

Figure 8 (Color online) Double-directional path loss distributions in the AoA-AoD plane with sounding bandwidth of 200 MHz. (a) 27.5 GHz, O-RX 1; (b) 27.5 GHz, O-RX 2; (c) 39.5 GHz, O-RX 1; (d) 39.5 GHz, O-RX 2.

BSs, in a way, is unable to provide stable links between BSs and mobile users. Consequently, installing a local area BS within each enclosed room or communicating with the help of relay is acceptable to lower outage probability with optimal mmWave network deployment.

4.2 Double-directional spatial propagation characteristics

In this subsection, directional propagation characteristics in the O2I scenario will be discussed because beamforming techniques will most likely be employed to provide high-gain directional beams for establishing reliable links between BSs and mobile users when using large-scale antenna arrays [7].

Figure 8 depicts the distribution of the directional path loss in the AoA-AoD plane. By comparing measurement results at O-RX 1 and 2 using identical configurations, the directions of the dominant paths with the lowest directional path loss are $\phi_{\mathrm{TX}} = 145^\circ$ and $\phi_{\mathrm{RX}} = 30^\circ$ for O-RX 1 and $\phi_{\mathrm{TX}} = 155^\circ$ and $\phi_{\mathrm{RX}} = 300^\circ$ for O-RX 2, both of which coming from the orientation of the double-pane glass window. Such a consistency with the spatial distribution of omnidirectional BELs in the office indicates that more strong signals will be transmitted from an outdoor BS into a building with a larger window-to-wall ratio. Generally, there is a dominant path along the T-R boresight-to-boresight pointing angle, and only a few reflections (e.g., $\phi_{\mathrm{RX}} \in [200^\circ, 330^\circ]$ for O-RX 1) from surrounding structures can be detected. According to Figure 8, directional path loss at 39.5 GHz is on average 10 dB higher than that at 27.5 GHz. Notice that the effective signals distributed in the AoD plane mainly concentrate in a small angular region. Thus, downlink beamforming is cost-effective for O2I coverage, while most signals will be blocked by external walls if wide-beam antennas are employed for sector coverage. Consequently, beamspace representation is a natural choice for characterizing the O2I channel.

Table 4 identifies the statistics of the ASA and ASD, calculated following the definitions in (5)–(8). In agreement with the results for the I2I channels, the mean values of the ASA and ASD decrease with increasing carrier frequency, which are fundamental physical phenomena in radio propagation in the mmWave band. Note that the differences in the ASA and ASD with RF bandwidths of 200 MHz and 600 MHz are abrupt at 39.5 GHz, whereas only a slight difference can be observed at 27.5 GHz. To our conjecture, this is because the power of most MPCs is lower than the detection level of the sounder with a specific configuration, and thus limited MPCs can be extracted at 39.5 GHz. Figure 9 depicts the ratio of the combined received power of the top N directional beams to the total received power in percentage terms:

$$\eta_N = \frac{\sum_{k=1}^{N} p_k}{\sum_{k=1}^{K} p_k}, \tag{11}$$

where p_k is the kth directional beam power ordered from strongest to weakest computed following (1) and K ($K \geqslant N$) is the total number of effective paths. For O2I measurements, K is equal to $6 \times 3 \times 36$ for all double-directional beam combinations. It can be seen that the 27.5 GHz channel with RF bandwidths of 200 and 600 MHz as well as the 39.5 GHz channel with an RF bandwidth of 200 MHz have the same

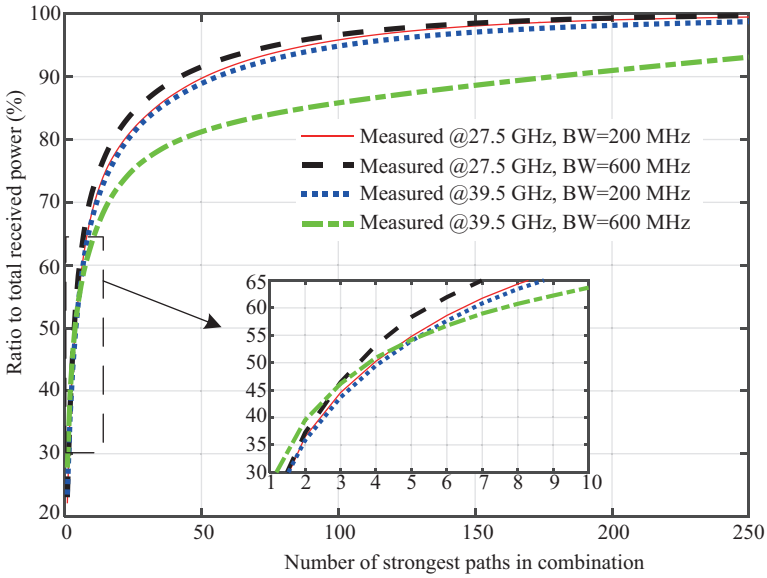

Figure 9 (Color online) Power ratio of the combined directional beam to the total varying with the number of strongest paths in combination.

shape as their curves, showing that η_N sharply peaks in the region of 1–50 and levels off after combining the top 50 strongest paths. To ensure that 90% of the total received power has been combined, at least 178 effective paths need to be combined for the 39.5 GHz channel with an RF bandwidth of 600 MHz, whereas only 42, 51, and 56 effective paths are needed for the other three cases, confirming the fact that beam combining in the azimuthal and elevation directions is critical to reducing the interference power in the O2I scenario at higher frequencies. As shown by the inset in Figure 9, η_N (i.e., green line) is slightly larger than those obtained at both frequency bands with an RF bandwidth of 200 MHz (i.e., red and blue lines) in the region of 1–4 with respect to the number of strongest beams being combined. Intuitively, this trend is consistent with the empirical RMS ASA and ASD summarized in Table 4, revealing that a smaller range of composite angular spread values corresponds to more concentrated received signals in a relatively limited angular range.

5 Conclusion

MmWave communication supports the explosive demands for ultra-high data rates in 5G and beyond cellular systems. In this work, extensive field measurement results varying with frequency, bandwidth, and transceiver siting in I2I and O2I scenarios have been shown. Because of the high-efficiency and flexible mmWave channel sounder, omnidirectional and directional channel characteristics can be simultaneously obtained.

To predict the mmWave I2I coverage, a dual-slope path loss model with a BP distance is developed, where greater step loss can be observed in scenarios with LoS to the completely blocked NLoS transition region in comparison with the case from the shadow region. In the O2I scenario, the BEL is mainly affected by the building structure and the relative locations of RXs with respect to the external wall (i.e., window position and window-to-wall ratio), where unfavorable propagation results in severe BELs with RX moving farther away from TX. Considering directional propagation characteristics for I2I and O2I channels, beam combining at RX sides is necessary, where more beams need to be synthesised for indoor NLoS coverage due to the larger ASA as well as O2I coverage at higher frequencies. Meanwhile, empirical analysis shows that large-scale fading (i.e., path loss, BEL, and angular spread) is bandwidth-independent, whereas the delay spread generally increase with increasing bandwidth. This work provides major insights into system designs that may facilitate the deployment of cost-effective mmWave mobile communication cellular networks.

Acknowledgements This work was supported in part by National Key R&D Program of China (Grant No. 2018YFB1801101), National Natural Science Foundation of China (Grant Nos. 61960206006, 61671145), and Key R&D Program of Jiangsu Province of China (Grant No. BE2018121).

References

1 Rappaport T S, Sun S, Mayzus R, et al. Millimeter wave mobile communications for 5G cellular: it will work! IEEE Access, 2013, 1: 335–349
2 Shafi M, Molisch A F, Smith P J, et al. 5G: a tutorial overview of standards, trials, challenges, deployment, and practice. IEEE J Sel Areas Commun, 2017, 35: 1201–1221
3 Xiao M, Mumtaz S, Huang Y M, et al. Millimeter wave communications for future mobile networks. IEEE J Sel Areas Commun, 2017, 35: 1909–1935
4 Li L M, Wang D M, Niu X K, et al. mmWave communications for 5G: implementation challenges and advances. Sci China Inf Sci, 2018, 61: 021301
5 Andrews J G, Bai T, Kulkarni M, et al. Modeling and analyzing millimeter wave cellular systems. IEEE Trans Commun, 2017, 65: 403–430
6 Ramirez D, Huang L, Wang Y, et al. On opportunistic mmWave networks with blockage. IEEE J Sel Areas Commun, 2017, 35: 2137–2147
7 Roh W, Seol J Y, Park J, et al. Millimeter-wave beamforming as an enabling technology for 5G cellular communications: theoretical feasibility and prototype results. IEEE Commun Mag, 2014, 52: 106–113
8 Heath R W, Gonzalez-Prelcic N, Rangan S, et al. An overview of signal processing techniques for millimeter wave MIMO systems. IEEE J Sel Top Signal Process, 2016, 10: 436–453
9 Ghatak G, de Domenico A, Coupechoux M. Coverage analysis and load balancing in hetnets with millimeter wave multi-RAT small cells. IEEE Trans Wirel Commun, 2018, 17: 3154–3169
10 Rappaport T S, MacCartney G R, Samimi M K, et al. Wideband millimeter-wave propagation measurements and channel models for future wireless communication system design. IEEE Trans Commun, 2015, 63: 3029–3056
11 Rappaport T S, Xing Y, MacCartney G R, et al. Overview of millimeter wave communications for fifth-generation (5G) wireless networks — with a focus on propagation models. IEEE Trans Antenna Propag, 2017, 65: 6213–6230
12 Wang C X, Bian J, Sun J, et al. A survey of 5G channel measurements and models. IEEE Commun Surv Tut, 2018, 20: 3142–3168
13 Huang J, Wang C X, Liu Y, et al. A novel 3D GBSM for mmWave MIMO channels. Sci China Inf Sci, 2018, 61: 102305
14 Yin X F, Ling C, Kim M D. Experimental multipath-cluster characteristics of 28-GHz propagation channel. IEEE Access, 2015, 3: 3138–3150
15 Maccartney G R, Rappaport T S, Sun S, et al. Indoor office wideband millimeter-wave propagation measurements and channel models at 28 and 73 GHz for ultra-dense 5G wireless networks. IEEE Access, 2015, 3: 2388–2424
16 Raghavan V, Partyka A, Akhoondzadeh-Asl L, et al. Millimeter wave channel measurements and implications for PHY layer design. IEEE Trans Antenna Propag, 2017, 65: 6521–6533
17 Zhang P Z, Wang H B, Wang H M, et al. Cluster-based analysis of wideband millimeter-wave channel for corridor environment. In: Proceedings of Asia-Pacific Conference on Antennas and Propagation, Xi'an, 2017
18 Zhang P Z, Li J, Wang H B, et al. Indoor small-scale spatiotemporal propagation characteristics at multiple millimeter-wave bands. Antennas Wirel Propag Lett, 2018, 17: 2250–2254
19 Senic J, Gentile C, Papazian P B, et al. Analysis of E-band path loss and propagation mechanisms in the indoor environment. IEEE Trans Antenna Propag, 2017, 65: 6562–6573
20 Rappaport T S, Heath R W, Daniels R C, et al. Millimeter Wave Wireless Communications. Englewood Cliffs: Prentice Hall, 2014. 123–146
21 Anderson C R, Rappaport T S. In-building wideband partition loss measurements at 2.5 and 60 GHz. IEEE Trans Wirel Commun, 2004, 3: 922–928
22 Zhao H, Mayzus R, Sun S, et al. 28 GHz millimeter wave cellular communication measurements for reflection and penetration loss in and around buildings in New York city. In: Proceedings of IEEE International Conference on Communication, Budapest, 2013. 5163–5167
23 Karttunen A, Nguyenl S L H, Koivumaki P, et al. Window and wall penetration loss on-site measurements with three methods. In: Proceedings of European Conference on Antennas and Propagation, London, 2018
24 Vargas C E O, Mello L d S. Measurements of reflection and penetration loss of construction materials at 28 GHz and 38 GHz. In: Proceedings of IEEE-APS Topical Conference on Antennas and Propagation in Wireless Communications, Xi'an, 2018. 897–900
25 Du Y S, Cao C, Zou X F, et al. Measurement and modeling of penetration loss in the range from 2 GHz to 74 GHz. In: Proceedings of IEEE Globecom Workshops, Washington, 2016
26 ITU-R. Effects of Building Materials and Structures on Radiowave Propagation Above about 100 MHz. ITU-R Technical Report P.2040-1. 2015
27 Inomata M, Sasaki M, Onizawa T, et al. Effect of reflected waves from outdoor buildings on outdoor-to-indoor path loss in 0.8 to 37 GHz band. In: Proceedings of International Symposium on Antennas and Propagation, Okinawa, 2016. 62–63
28 Imai T, Kitao K, Tran N, et al. Outdoor-to-indoor path loss modeling for 0.8 to 37 GHz band. In: Proceedings of

European Conference on Antennas and Propagation, Davos, 2016
29 Diakhate C A L, Conrat J, Cousin J, et al. Millimeter-wave outdoor-to-indoor channel measurements at 3, 10, 17 and 60 GHz. In: Proceedings of European Conference on Antennas and Propagation, Paris, 2017. 1798–1802
30 ITU-R. Prediction of Building Entry Loss. ITU-R Technical Report P.2109-0. 2017
31 3GPP. Study on Channel Model for Frequency from 0.5 to 100 GHz. 3GPP Technical Report 38.901 (V15.0.0). 2018
32 Lee J, Kim K, Kim M, et al. Empirical investigation of antenna beamwidth effects on the ITU-R building entry loss (BEL) model based on 32 GHz measurements. In: Proceedings of Global Symposium on Millimeter Waves, Boulder, 2018
33 Umit B C, Wang R, Sangodoyin S, et al. Outdoor to indoor propagation channel measurements at 28 GHz. IEEE Trans Wirel Commun, 2019, 18: 1477–1489
34 Li J, Zhang P, Wang H, et al. High-efficiency millimeter-wave wideband channel measurement system. In: Proceedings of European Conference on Antennas and Propagation, Krakow, 2019
35 ITU-R. Multipath Propagation and Parameterization of its Characteristics. ITU-R Technical Report P.1407-6. 2017
36 Zhang P Z, Li J, Wang H M, et al. Millimeter-wave space-time propagation characteristics in urban macrocell scenarios. In: Proceedings of IEEE International Conference on Communications, Shanghai, 2019
37 Wang H M, Zhang P Z, Li J, et al. Radio propagation and wireless coverage of LSAA-based 5G millimeter-wave mobile communication systems. China Commun, 2019, 16: 1–18
38 Samimi M K, Rappaport T S. 3-D millimeter-wave statistical channel model for 5G wireless system design. IEEE Trans Microw Theory Tech, 2016, 64: 2207–2225
39 Rappaport T S, MacCartney G R, Sun S, et al. Small-scale, local area, and transitional millimeter wave propagation for 5G communications. IEEE Trans Antenna Propag, 2017, 65: 6474–6490
40 Shafi M, Zhang J H, Tataria H, et al. Microwave vs. millimeter-wave propagation channels: key differences and impact on 5G cellular systems. IEEE Commun Mag, 2018, 56: 14–20
41 Fleury B H. First- and second-order characterization of direction dispersion and space selectivity in the radio channel. IEEE Trans Inf Theory, 2000, 46: 2027–2044
42 Du J F, Chizhik D, Feick R, et al. Suburban residential building penetration loss at 28 GHz for fixed wireless access. IEEE Wirel Commun Lett, 2018, 7: 890–893